LEIDEN UNIVERSITY

Study of BCG-Substracted Images of Nearby Clusters

by

Juan Manuel Espejo Salcedo

Advisor:

Dr. Henk Hoekstra

Natural Sciences Faculty
Sterrenwacht

June 2017

"Not only is the Universe stranger than we think, it is stranger than we can think.."

Werner Heisenberg

Abstract

Natural Sciences Faculty
Sterrenwacht

We study the center of deep imaging data of low redshift massive galaxy clusters where the light from the BGC overwhelms the images from background galaxies and faint cluster members in the cluster core. The proper subtraction of the BCG light is expected to reveal background galaxies that are strongly lensed. We constrain the number of objects that we expect to find in these systems and corroborate these results when subtracting the BCGs and analysing these central regions. Identifying such systems allows for unique follow-up studies regarding the stellar populations in the BCGs and thus their formation history. Also the number density of faint cluster members may tell us something about the dynamical state of the cluster and how BGCs form. The aim of this project is to model the BCG light and search for strong lensing candidates and study the properties of faint cluster members in the core.

Acknowledgements

I would like to thank . . .

Contents

List of Figures

Dedicated to my parents, whose love and support are my biggest motivation...

Chapter 1

Introduction

Understanding the formation history of stars allows us to comprehend many physical properties of their host galaxies thus providing a useful framework on which to build a more elaborate theory of their subsequent evolution. We might have good ideas and some general agreement in the basics of formation of stars in galaxies, but our observational limitations don't allow us to say much about distant objects which we need to make a more elaborate and complete theory. In principle, we can't assume that all populations of stars have the same formation history in every galaxy and for every epoch of the Universe. The molecular clouds (dense concentrations of interstellar gas and dust) that collapse gravitationally to form stars might or might not create the same mixture of stars in every stellar system since this depends strongly on their composition and the environment in which they collapse, so it is important to see under what conditions we could assume a general trend and what implications in our observations this may have.

For galaxies that are far away, it is impossible to make star counts with our current technology, for this reason, their mass-to-light-ratio Υ (which depends on their stellar populations) provides a simple constraint on their number of stars per unit mass given by the initial mass function (IMF), which is a very fundamental and important quantity in the study of stellar systems because it constraints the physics of star formation but also because it allows us to infer stellar masses through observed luminosities as discussed by Smith & Lucey (2013). Everything we know from galaxy evolution is implicitly assuming a certain form of the IMF with very little variations since it is the method we use to connect evolutionary sequences, this of course, given the fact that if every galaxy had its own IMF then it would be too difficult to study their evolution because of the lack of any knowledge about their history.

A satisfactory determination of the IMF in galaxies is a difficult task, since it depends on very reliable and well-understood data and calibrations and because is seems to be intimately dependent on the galaxys formation history (Cappellari et. al. 2012). The determination is usually made by observing star counts, getting the present-day luminosity function (assuming proper mass-luminosity relation and theoretical models that take into account the metallicity), getting the present-day mass function (for some evolutionary tracks and metallicities) and assuming some star formation history to get the IMF. All these assumptions, and the fact that extrapolating these results to systems in which we can't get star counts make the determination very complicated. Moreover, another difficulty of the determination of IMF is that the classical assumption of a single IMF covering the whole mass range is being questioned in favour of a two-component IMF to account for possible different formation modes.

Despite these difficulties, we have some observational information about IMFs in galaxies, in the case of spiral galaxies for example, the most commonly used IMFs are Chabrier (Chabrier 2003) and Kroupa (Kroupa 2001). With Kroupa favouring a higher number of stars in the low mass regime ($M < 0.5M_{\odot}$) as compared to Chabrier's. These IMFs are decently constrained given the facilities of our observations in our own galaxy. Also, bulges appear to have heavier IMFs than disks (such as the Salpeter IMF by Salpeter **?**) as mentioned by Brewer et. al. (2012).

Although these primary assumptions given by our limited observational evidence might not be too far from reality, we must note that when we study more complex and dense systems like the brightest cluster galaxies (BCG) in galaxy clusters or giant elliptical galaxies in general, constraining the IMF via $\mathrm{M}_{\star}/\mathrm{L}$ might be way more complex and poses a greater challenge since masses are more difficult to establish for dynamically-hot systems like them. Measuring Υ in these systems is not a truly accurate constraint on the IMF since we may have different stellar formation histories than the ones associated with galaxies that are being formed now. These objects have a very old origin (although their build up and morphological formation is recent) because their stellar populations are old and they correspond to the highest density peak, so it is difficult to relate their stellar populations accurately.

The $\mathrm{M}_{\star}/L$ depends on galaxy type, but due to the lack of multi-wavelength photometry, it is often assumed that all cluster galaxies are composed of the same stellar population. If one assumes an old stellar population (and therefore a high $\mathrm{M}_{\star}/L$), the mass of the late-type galaxies (and thus the cluster as a whole) is over-estimated (Van der Burg et. al. 2015).

Mass-to-light ratios of early-type galaxies are of particular interest to understand the tilt of the fundamental plane. Virial relations imply that the effective surface brightness I_{eff}, the effective radius r_{eff} and the central velocity dispersion σ_0 in hot stellar systems are not independent of each other. This is revealed by the fundamental plane of early type galaxies.

This general view shows that in the context of the evolution of galaxies, there are many things that come together at the very core of cosmology but also in the context of stellar astrophysics and they need to be consistent with each other. Addressing this problem is complex for many reasons, one of them is that these systems have a strong dependency on their non-baryonic matter content which affects the mass-to-light-ratio determination. This dark matter contribution accounts for most of the dynamical mass of galaxies and it's the dominant contribution in most of their spacial scales, specially in the outer regions. The problem would be much easier to study if we only had the stellar mass because the light measurements would be enough to constrain the stellar populations, their evolution and their mass distribution.

Being able to calculate the percentage of dark matter allows us to define the IMF more precisely. So we want to see what fraction of the surface density is given by stars and what are the spatial scales in which DM becomes the dominant contribution to the enclosed mass. DM halos seem to have a diluted profile in comparison to the stellar content of galaxies (Navarro Frenk & White 1996) so there is a region near the center of these massive systems in which the stellar mass is the dominant contribution. This implies that accurate measurements of their luminosity could give precise determinations of their mass to light ratio thus giving us some knowledge of their IMFs.

For stars, measurements of the luminosity function can be used to derive the Initial Mass Function (IMF). For galaxies, this is more difficult because Mass to light ratio (M/L) of the stellar population depends upon the star formation history of the galaxy. Bulges have heavier IMFs than disks. Recent studies have investigated how the IMF varies with galaxy mass, specially in elliptical galaxies. One of the methods used for this study is a rather indirect method, where galaxy stellar masses are determined from stellar population synthesis models that actually do not resolve the IMF, the results suggest that lower mass early-type galaxies (with dispersions $\sigma \approx 200$ km/s) seem to be consistent with a Milky-Way type IMF (e.g. a Kroupa or Chabrier IMF). In high-dispersion elliptical galaxies, however, stellar mass-to-light ratios are about a factor of 2 times higher than expected from a Kroupa IMF. Some studies indicate that the IMF in massive galaxies seems to be more dwarf dominated than in the Milky-Way so that they can be described by a Salpeter IMF (Thomas 2014). Figure [1.1] shows the dependence of the enclosed mass of a galaxy on different IMFs.

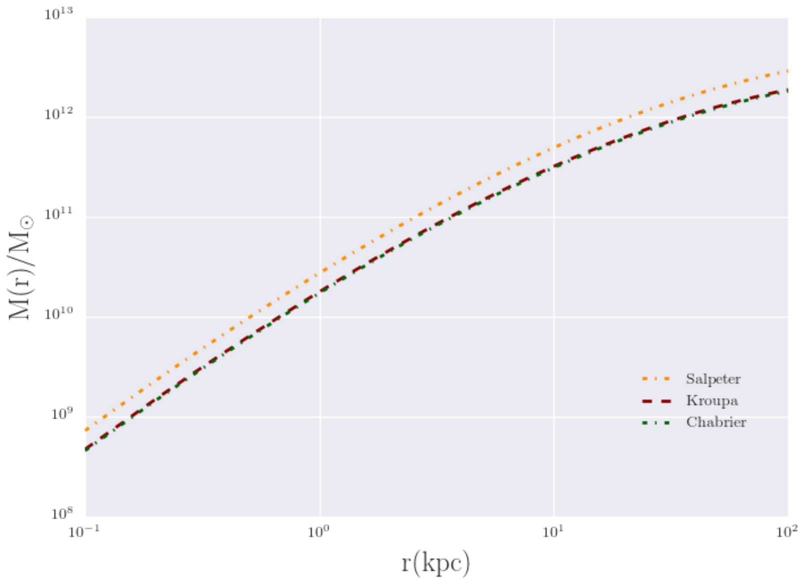

FIGURE 1.1: Enclosed mass for different IMFs in a galaxy of $M_{200} \approx 10^{12} M_\odot$

Various techniques have been developed to try to understand the stellar populations that form these massive systems. One of them is by using gravitational lensing of background galaxies (Treu et. al. 2010). Modelling the lensing configuration on a BCG provides a useful method to determine stellar and dark matter mass contribution in elliptical galaxies, since it is difficult to constraint the IMF via $M_\star/L$ as mentioned before. Finding strong lensing in these systems can also give us information about the location of the mass center of the cluster through the lensing they produce. We usually assume that the centre of galaxy clusters lies in the BCGs (George et. al. 2012) but the real position of the centre in galaxy clusters is still an unsolved problem (Harvey et. al 2017).

Strong lensing measures exactly the enclosed mass so we need to know how much of its contribution we need to subtract, the less we have to subtract, the better for the determination of the IMF. If the effect of the IMF is very subtle in the mass vs radius plot, then we would need to know the dark matter distribution very well, but if the effect of the IMF is not very subtle, the less we need to know about the dark matter distribution. A recent study of a BCG mentions the relevance of this spatial scale, at very small radii stars dominate the lensing mass, so that lensing provides a direct probe of the stellar mass-to-light ratio, with only small corrections needed for dark matter (Smith & Lucey 2013).

In this project we work with galaxy clusters that might be in the right range to search for gravitational lensing in the inner regions. We use deep data from CFHT that allows us to search for interesting targets and probe the relevant spacial scales. We focus on the brightest cluster galaxy since it is a very massive system that could lens background objects and because photometry measurements can be made very accurately on them in comparison with their neighbouring galaxies.

Chapter 2

Introduction to Gravitational Lensing

One of the most interesting consequences of Einstein's theory of General Relativity, regarding the distortion of space time by massive objects is gravitational lensing. The basic principle behind gravitational lensing is that light is distorted when it travels close to the potential well (the distortion of space time) of massive objects which is an analogous effect to the one caused by optical lenses.

Although the discovery of gravitational lensing was made only in the past century, the possibility that there could be such a deflection had been suspected much earlier, by Newton and Laplace among others (Narayan et. al. 1995). Johann Gerog von Soldner in 1801 calculated the magnitude of the deflection due to the Sun, assuming that light consists of material particles and using Newtonian gravity. Later, Einstein (1911) employed the equivalence principle to calculate the deflection angle and re-derived Soldners formula. Later yet, in 1915 Einstein applied the full field equations of General Relativity and discovered that the deflection angle is actually twice his previous result, the factor of two arising because of the curvature of the metric. According to this formula, a light ray which tangentially grazes the surface of the Sun is deflected by 1.7". Einsteins final result was confirmed in 1919 when the apparent angular shift of stars close to the limb of the Sun (see Fig. [1]) was measured during a total solar eclipse in 1920. The quantitative agreement between the measured shift and Einsteins prediction was immediately perceived as compelling evidence in support of the theory of General Relativity.

Gravitational lensing can be separated into two main categories which are its two most important ways to manifest.

1. Strong lensing: Where there are easily visible distortions such as the formation of Einstein rings, arcs, and multiple images.

2. Weak lensing: Where the distortions of background sources are much smaller and can only be detected by analysing large numbers of sources in a statistical way to find coherent distortions of only a few percent.

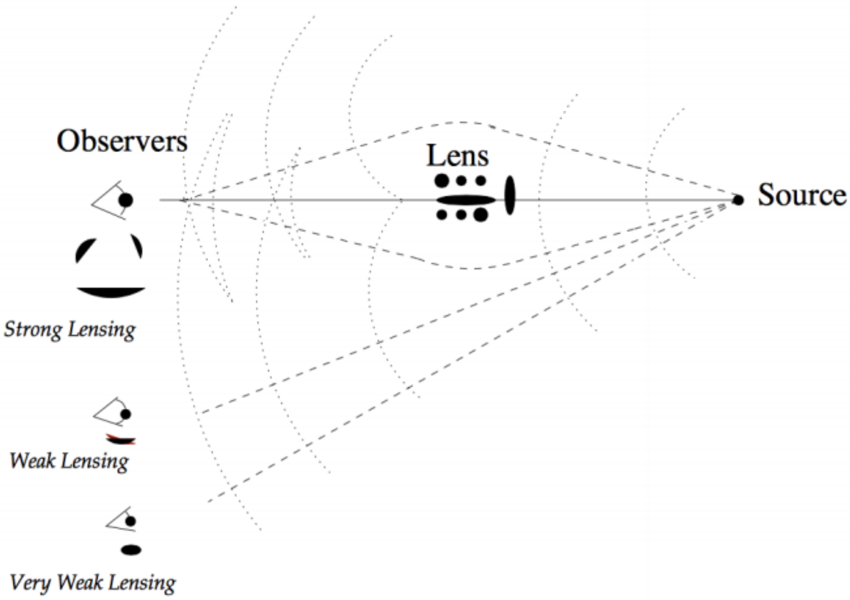

FIGURE 2.1: Types of lensing. Courbin et. al. 2002

Figure [2.1] sketches the effects of gravitational lensing in the strong, weak and very weak lensing regimes. As seen in the figure, under certain conditions the background source can be seen in multiple images and "arcs" surrounding the lensing object, which is the strong lensing regime and will be the useful regime for this work.

2.1 Gravitational Lensing formalism

For the generalities of gravitational lensing we follow the order given in a review by Meneghetti (2003) in which we first start by introducing the deflection angle which is the measure of the angular distance that has been deflected and which is linearly dependent on the mass M. This dependence ensures that the angles of deflection of an array of lenses can be superposed linearly. If we had N point masses sparsed on a plane, with positions ξ_i and masses M_i, then the deflection angle would be:

$$\hat{\vec{\alpha}}(\vec{\xi}) = \sum_i \hat{\vec{\alpha}}_i(\vec{\xi} - \vec{\xi}_i) = \frac{4G}{c^2} \sum_i M_i \frac{\vec{\xi} - \vec{\xi}_i}{\left|\vec{\xi} - \vec{\xi}_i\right|^2} \tag{2.1}$$

Fortunately, in most three dimensional distributions of matter (even in the case of lensing by massive objects like galaxy clusters) the physical size of the lens is generally much smaller than the distances between the observer, the lens and the source. This means that the deflection of light takes place in a very thin and short section of its path to the observer. Given this, we can use the *thin screen approximation*: "The lens is approximated by a planar distribution of matter, the lens plane". Also the sources can be treated as if they lie on a plane which is called the source plane.

The *thin screen approximation* alows us to state that the lensing matter distribution is fully described by its surface density

$$\Sigma(\vec{\xi}) = \int \rho(\vec{\xi}, z) dz \tag{2.2}$$

where $\vec{\xi}$ is a two-dimensional vector on the lens plane and ρ is the three dimensional density.

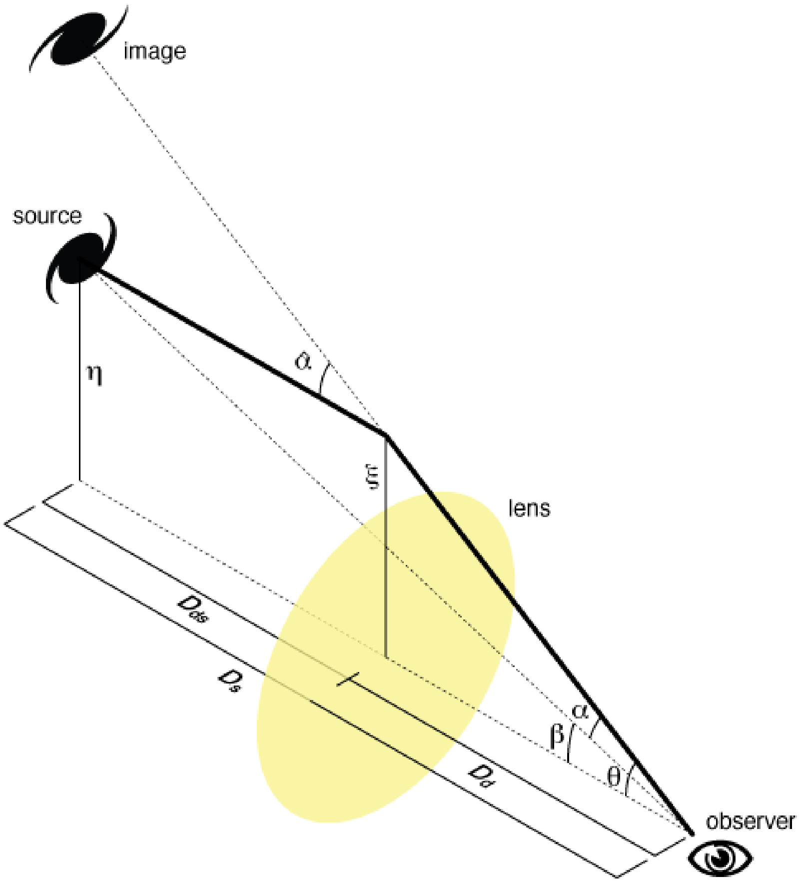

FIGURE 2.2: Sketch of a lensing configuration, where D_{ds} is the distance from the lense to the source, D_s is the distance from the observer to the source and D_d is the distance from the observer to the source. Image by Michael Sachs, Wikipedia.

Figure [2.2] is a sketch of a typical gravitational system. The lensing mass is located at a angular diameter distance D_d and it deflects the light rays coming from a source at an angular distance of D_s.

The optical axis is perpendicular to the lens and source planes and passes through the observer. We measure the angular positions on both planes with respect to this reference direction. The source is at the angular position $\vec{\beta}$ and lies on the source plane at a distance $\vec{\eta} = \vec{\beta} D_s$ from the optical axis. The deflection angle $\hat{\vec{\alpha}}$ of the light ray comes from the source and has impact parameter $\vec{\xi} = \vec{\theta} D_d$ on the lens plane. Due to this deflection, the observer receives the light coming from the source as if it was emitted at the angular position $\vec{\theta}$.

If $\vec{\theta}$, $\vec{\beta}$ and $\hat{\vec{\alpha}}$ are small, the true position of the source and its observed position on the sky are related by a very simple relation, obtained by a geometrical construction. This relation is called the lens equation and is written as

$$\vec{\theta} D_s = \vec{\beta} D_s + \hat{\vec{\alpha}} D_{ds} \tag{2.3}$$

where as seen in the figure, D_{ds} is the distance between the lens and the source.

Defining the reduced deflection angle

$$\vec{\alpha}(\vec{\theta}) \equiv \frac{D_{ds}}{D_s} \hat{\vec{\alpha}}(\vec{\theta}) \tag{2.4}$$

And from equation 2.3 we get

$$\vec{\beta} = \vec{\theta} - \vec{\alpha}(\vec{\theta}) \tag{2.5}$$

The most interesting physics of the simple lens equation arises because $\vec{\alpha}$ depends on $\vec{\theta}$. Now, we can characterize an extend the distribution of matter by its effective lensing potential, which is obtained by projecting the three-dimensional Newtonian potential on the lens plane and scaling it accordingly

$$\hat{\Psi}(\vec{\theta}) = \frac{D_{ds}}{D_d D_s} \frac{2}{c^2} \int \Phi(D_d \vec{\theta}, z) dz \tag{2.6}$$

This lensing potential satisfies two important properties:

1) The gradient of Ψ gives the scaled deflection angle:

$$\vec{\nabla}_x \Psi(\vec{x}) = \vec{\alpha}(\vec{x}) \tag{2.7}$$

2) The Laplacian of Ψ gives twice the convergence

$$\Delta_x \Psi(\vec{x}) = 2\kappa(\vec{x}) \tag{2.8}$$

where the convergence is defined as a dimensionless surface density

$$\kappa(\vec{x}) \equiv \frac{\Sigma(\vec{x})}{\Sigma_{cr}} \qquad \text{with} \qquad \Sigma_{cr} = \frac{c^2}{4\pi G} \frac{D_s}{D_d D_{ds}} \tag{2.9}$$

Σ_{cr} is called the critical surface density and it characterizes the lens system and which is a function of the angular diameter distances of lens and source. It is also very useful to quantify the distortion of shapes of background objects since it can be studied using statistical approaches on the observations, it is then useful to introduce the mathematical formalism of the distortion. One of the main features of gravitational lensing is that it distorts the shapes of the sources, this is particularly evident when the source has no negligible apparent size. In some cases the background galaxies can appear as very long arcs in galaxy clusters as mentioned at the beginning of this chapter.

The effect of distortion takes place because light bundles are deflected differentially. In the ideal case, the shape of the background images can be determined by solving the lens equation for all the points within the extended source. In particular, if the source is much smaller than the angular size on which the physical properties of the lens change, the relation between the source and image positions can locally be linearised. Mathematically this means that the distortion of images can be described by the Jacobian matrix

$$A \equiv \frac{\partial \vec{y}}{\partial \vec{x}} = \left(\delta_{ij} - \frac{\partial \alpha_i(\vec{x})}{\partial x_j}\right) = \left(\delta_{ij} - \frac{\partial^2 \Psi(\vec{x})}{\partial x_i \partial x_j}\right) \tag{2.10}$$

where x_i indicates the i-component of $\vec{x}$ on the lens plane. It shows that the elements of the Jacobian matrix can be written as combinations of the second derivatives of the lensing potential. It is useful to use the shorthand notation

$$\frac{\partial^2 \Psi(\vec{x})}{\partial x_i \partial x_j} \equiv \Psi_{ij} \tag{2.11}$$

Now, by splitting off an isotropic part from the Jacobian

$$\left(A - \frac{1}{2}\mathrm{tr}A \cdot I\right)_{ij} = \begin{pmatrix} -\frac{1}{2}\left(\Psi_{11} - \Psi_{22}\right) & -\Psi_{12} \\ -\Psi_{12} & \frac{1}{2}\left(\Psi_{11} - \Psi_{22}\right) \end{pmatrix} \tag{2.12}$$

we get the shear matrix, which is an antisymmetric, trace-free matrix that quantifies the projection of the gravitational tidal field (the gradient of the gravitational force), which describes distortions of background sources. This allows us to define the pseudo-vector $\vec{\gamma} = (\gamma_1, \gamma_2)$ on the lens plane, whose components are

$$\gamma_1(\vec{x}) = \frac{1}{2}(\Psi_{11} - \Psi_{22}) \qquad \text{and} \qquad \gamma_2(\vec{x}) = \Psi_{12} = \Psi_{21} \tag{2.13}$$

This is called the shear. The eigenvalues of the shear matrix are

$$\pm\sqrt{\gamma_1^2 + \gamma_2^2} = \pm\gamma \tag{2.14}$$

Thus, there exists a coordinate rotation by an angle ϕ such that

$$\begin{pmatrix} \gamma_1 & \gamma_2 \\ \gamma_2 & -\gamma_1 \end{pmatrix} = \gamma \begin{pmatrix} \cos 2\phi & \sin 2\phi \\ \sin 2\phi & -\cos 2\phi \end{pmatrix} \tag{2.15}$$

And for the trace we have

$$\frac{1}{2}\mathrm{tr}A = (1-\kappa)\delta_{ij} \tag{2.16}$$

Thus the Jacobian becomes

$$A = \begin{pmatrix} 1-\kappa-\gamma_1 & -\gamma_2 \\ -\gamma_2 & 1-\kappa+\gamma_1 \end{pmatrix} \tag{2.17}$$

Where κ is the convergence that determines the magnification and γ_1 and γ_2 are the shear components that determine the distortion of the background objects. More precisely, the convergence describes the isotropic focusing of light rays while the shear describes the effect of tidal gravitational forces. Convergence acting alone leads to an isotropic magnification or demagnification while the shear induces distortions in the shapes of lensed images (Wright & Brainerd 1999).

Finally, we can introduce another useful quantity in the characterization of gravitational lensing systems. The *magnification* is quantified by the inverse of the determinant of the Jacobian matrix. For this reason, the matrix $\mathrm{M} = A^{-1}$ is called the *magnification tensor*, and we define

$$\mu \equiv \mathrm{det}M = \frac{1}{\mathrm{det}A} = \frac{1}{(1-\kappa)^2 - \gamma^2} \tag{2.18}$$

The eigenvalues of the magnification tensor measure the amplification in the tangential and in the radial direction and are given by

$$\mu_t = \frac{1}{\lambda_t} = \frac{1}{1-\kappa-\gamma} \qquad \text{and} \qquad \mu_r = \frac{1}{\lambda_r} = \frac{1}{1-\kappa+\gamma} \tag{2.19}$$

The magnification is ideally infinite where $\lambda_t = 0$ and where $\lambda_r = 0$. These two conditions define two curves in the lens plane, called the tangential and the radial critical line, respectively. An image forming along the tangential critical line is strongly distorted tangentially to this line. On the other hand, an image forming close to the radial critical line is stretched in the direction perpendicular to the line itself.

In the inner region of galaxy clusters we are in the strong lensing regime so we will focus our discussion on strong lensing and the search for multiple images and arcs in the inner regions of the galaxy clusters. Figure [2.3] is a representation of a lensing system in which a background galaxy is lensed by a cluster of galaxies and produces multiple images and arcs observed by our telescopes.

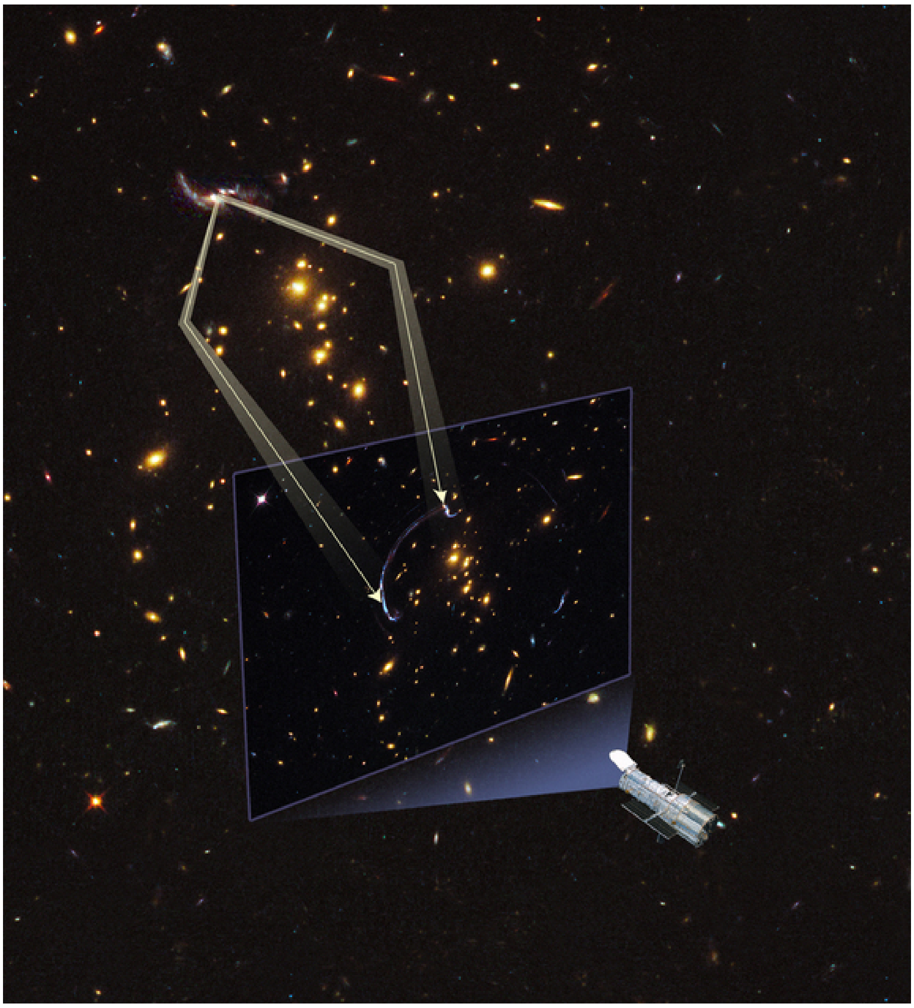

FIGURE 2.3: Representation of strong lensing by a galaxy cluster. Credits to NASA.

Now, let's understand in what scales we can use gravitational lensing to study these massive systems.

Chapter 3

Determination of the relevant scales

Figure [3.1] shows a composite image of a galaxy cluster taken by the HST in which many lensed objects can be seen as distorted shapes and multiple images. The galaxy cluster MACS 1206 lies 4 billion light-years from Earth. In this system, astronomers counted 47 multiple images of 12 newly identified galaxies.

This galaxy cluster is part of the CLASH survey which among other ambitions, is searching for high accumulations of dark matter in their central cores which may yield new clues to the early stages in the origin of structure in the universe. This and other results suggest that dark matter is more densely packed inside clusters than some models predict and might as well mean that galaxy cluster assembly began earlier than commonly thought. Let's search for some insights into these problems.

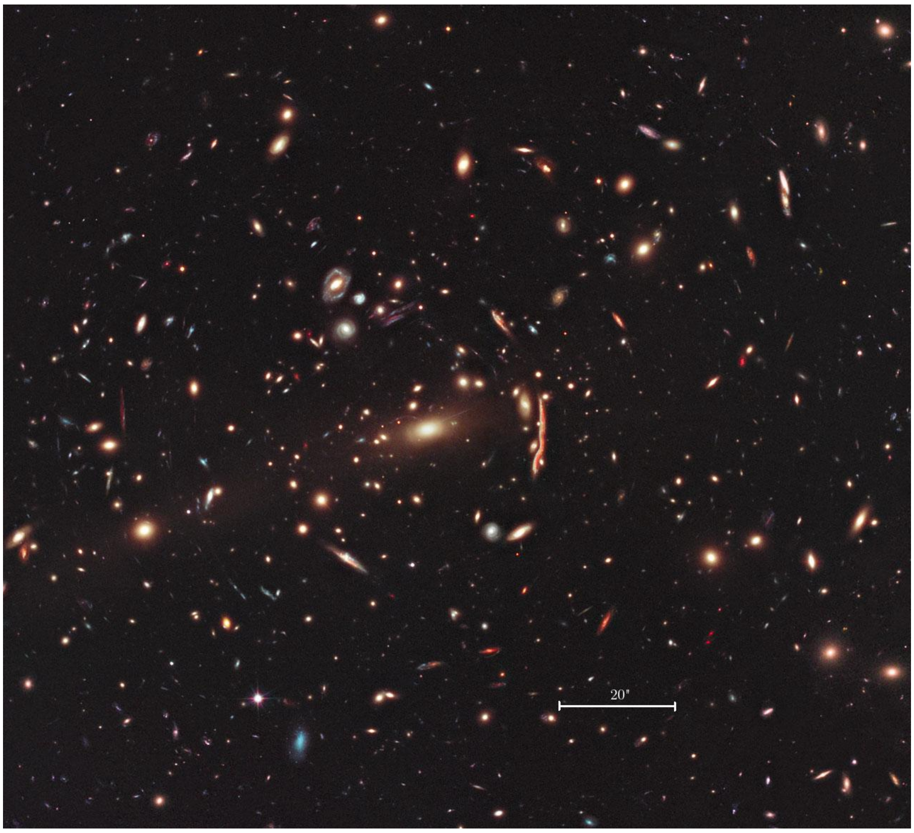

FIGURE 3.1: Galaxy Cluster MACS 1206 (z=0.439), credits to NASA Hubble Space Telescope.

In this project we base our analysis on the center of galaxy clusters at low redshift so it is necessary to understand which scales will be relevant for our studies. In order to calculate the range of scales that we will probe in the observational procedures on Chapter 4 we will do two separate experiments. The first one is the study of the number of objects that we would expect to be lensed near the cluster centres by using a very extensive catalogue of galaxies (this will suggest how many objects we expect in the vicinity of the BCGs). The second one consists on doing the mass modelling of the cluster for its stellar and dark matter content to see on which scale stars are the main component of the enclosed mass that lenses background objects (this will suggest where the determination and characterisation of the IMF can be done with a good degree of confidence).

3.1 COSMOS field

For our first experiment, we make use of the COSMOS2015 catalogue (Laigle et. al. 2016) which contains half a million objects in a range of $1 < z < 6$. Ricardo Herbonnet matched the CFHT data to this catalogue so we use his matched data which contains a total of 133,348 galaxies in the 2 degree COSMOS field. We count the amount of galaxies for different magnitudes in redshift bins of $0.2z$ for the r filter. These numbers represents the expected number of galaxies in the background of the lens objects of our sample as seen in figure [3.2].

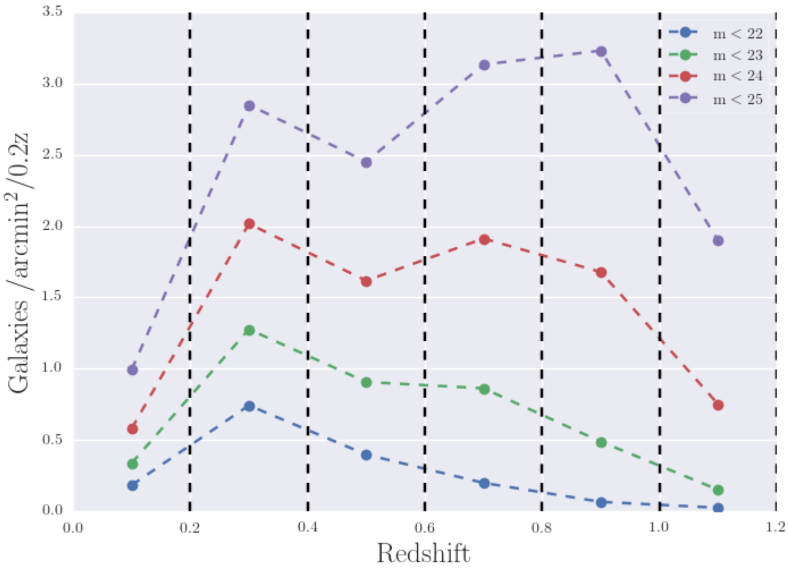

FIGURE 3.2: Galaxies per arcmin^2 in redshift bins of $0.2z$ for different magnitudes. HST could be able to see objetcs with magnitudes below 25 while CFHT can see objects with magnitudes around 23.

Around $z = 0.3$ we find the peak for the number of galaxies so it is the redshift that is most likely to contain galaxies that could be seen in our data. For the depth of our data of around 23 mag (as discussed in the next chapter) we then expect some background galaxies lensed by the BCGs and for which we can measure the Einstein ring, although the number is rather small.

CFHT can see objects as deep as $m = 23$ but Hubble Space Telescope could see objects with $m = 25$ so it should be able to see a lot more objects that have been lensed. This result is a first suggestion that within the inner region of the galaxy clusters, there must be lensed objects in the form of arcs or multiple images that we could be able to see with our sample making a careful subtraction of the BCG light. Now we must answer the question regarding the scales in which the stellar content (associated to the extracted light from the BCG) is relevant.

3.2 DM to stellar ratio

We first need to take into consideration is the density profile that we will use for our calculation of the fraction of DM and stellar light. The first usual approach for the density profile of the gravitational lens is an isothermal sphere (see Appendix), although in reality, the density profile and lensing properties of galaxies is a bit more complicated than the assumption of a SIS (singular isothermal sphere), so we need to take into account more complex but elaborate profiles such as the NFW (Navarro, Frenk & White 1996) which is an approximation to the equilibrium configuration of dark matter produced in N-body simulations of colissionless dark matter particles (see Appendix for the formalism of the NFW and it's lensing equations).

So for our second experiment proposed at the beginning of the chapter, we will use the galaxy cluster Abell 1068, located at a distance of $z = 0.138$ with magnitudes in U=21.94, i=18.46, g=20.09, r=19.5, also $M_{200} = 4.3 \times 10^{14} M_{\odot}$ (Van der Burg et. al. 2015) and calculate its NFW dark matter halo profile (since galaxy clusters are known to be dominated by their dark matter content) and at the same time we calculate its stellar mass profile using the de Vaucouleurs surface brightness profile by de Vaucouleurs (1948) which is a specific case of a Sersic's more general profile. This allows us to compare the contribution of stars in comparison to dark matter and thus see in which scales the DM mass becomes dominant thus making it more difficult to constrain the stellar content of the bright galaxy.

The concentration parameter for the NFW profile of this cluster is $c = 4.46$ (using Figure [1] in the Appendix). The critical density is 212 $M_{\odot}/\mathrm{kpc}^3$. The Hubble parameter at z=0.138 is H(z)=85.6. For an effective radius of $R_e = 73.7$ kpc we get a characteristic radius of $r_{1/2} = 307.1$.

For the stellar content of the cluster we can use de Vaucouleurs law for the surface brightness distribution in giant elliptical galaxies which is:

$$I(R) = I_e e^{-b\left[(R/R_e)^{1/4}-1\right]} \tag{3.1}$$

where $b = 7.67$ and I_e is the effective brightness which is basically the brightness at the effective radius R_e

For constant mass-to-light-ratio we have $\Sigma_{\star}(R) = \Upsilon I(R)$ (Lokas & Mamon 2001) where $I(R) \approx 10^7 M_{\odot}/\mathrm{kp}^2$ was found by fitting the surface brightness with `GALFIT` (as will be discussed in the next chapter). The mass to light ratio for a Salpeter IMF is $\Upsilon \approx 4$ so the stellar mass profile can be easily calculated with $\Sigma_{\star}(R) = 4I(R)$. The bolometric luminosity of Abell 1068 is 10^{44}erg/s that in solar luminosities is $1.9 \times 10^{12} L_{\odot}$, this gives an effective brightness of $0.962 \times 10^{7} \mathrm{M}_{\odot}/\mathrm{kpc}^2$.

Hence we have the surface mass density for both the stellar content and the NFW profile, as shown in Figure [3.3].

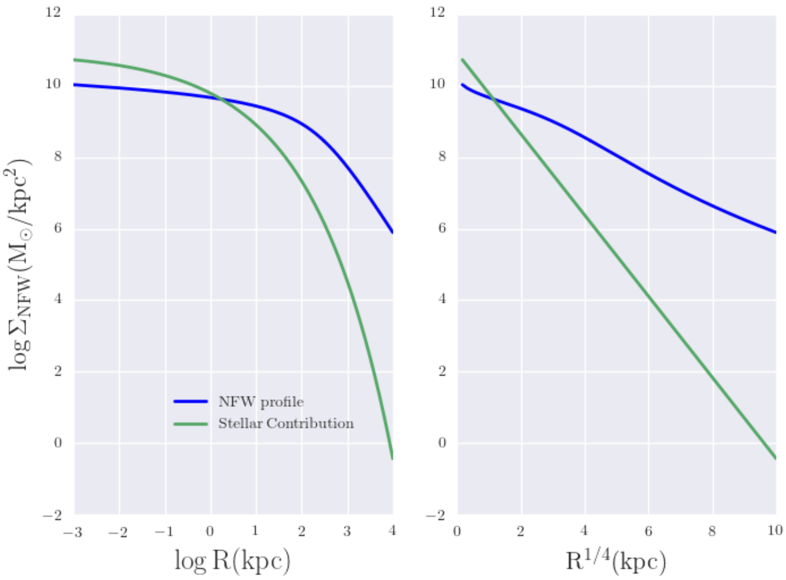

FIGURE 3.3: Surface mass density profiles in logarithmic and $R^{1/4}$ scale for the NFW profile and the stellar component.

But we are interested in the enclosed mass which can be found by integrating the surface densities. For the DM halo:

$$M(R) = 2\pi \int_0^R R\Sigma(R) dR \tag{3.2}$$

We can recover the luminosity by integrating the surface brightness profile accordingly:

$$L = 2\pi \int_0^R RI(R) dR \tag{3.3}$$

Let's introduce the dependence on different IMFs, mainly Salpeter, Chabrier and Kroupa. Salpeter initial mass function is of the form $n(\mathrm{M}) \propto \mathrm{M}^{-2.3}$ and implies that more low-mass stars and a higher mass-to-light ratio so for massive galaxies Salpeter is a good IMF.

In the R-band the scaling between the three IMFs is $\Upsilon_{\mathrm{Krou}} \approx 0.67\Upsilon_{\mathrm{Salp}}$ for Kroupa and $\Upsilon_{\mathrm{Chabrier}} \approx 0.63\Upsilon_{\mathrm{Salp}}$ for Chabrier. The systematic variation of the IMF in early-type galaxies can be seen in Figure [2] from the Appendix. The integration for these different

IMFs give a value that is comparable to the one found using Faber-Jackson relation which is $L = \Upsilon \times \sigma^4$.

IMF/Method	Mass ($M_\odot$)
Salpeter	4.82×10^{12}
Kroupa	3.13×10^{12}
Chabrier	3.03×10^{12}
Faber-Jackson	2.2×10^{12}
DM Halo	4.63×10^{14}

The value found for the enclosed mass for the NFW profile is similar to the one found by Sifon et. al. (2015) of $4.3 \times 10^{14} M_\odot$.

Now let's analyse the radial profiles of these enclosed masses since it is the plot that shows what radial scale we need to probe. The enclosed mass profile for dark matter and stellar matter for the three chosen IMFs (Chabrier, Kroupa, Salpeter) is shown in Figure [3.4].

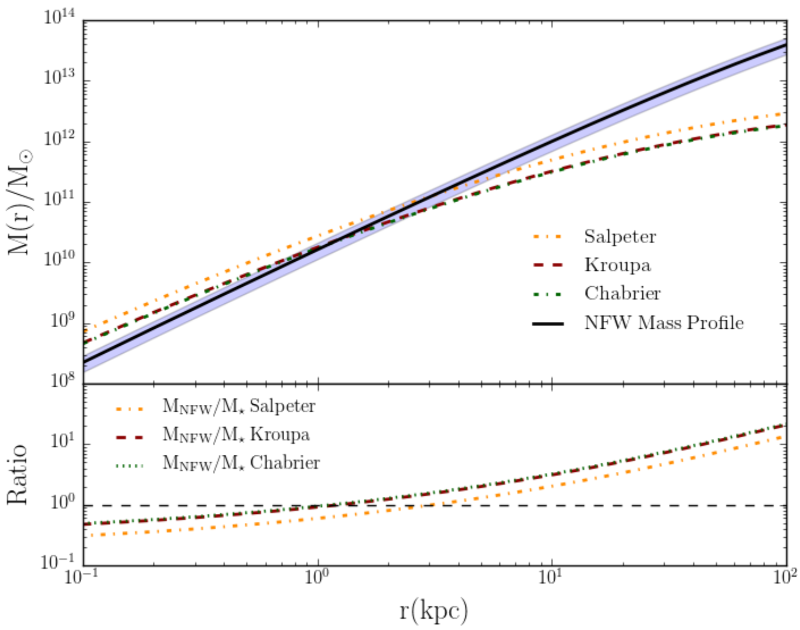

FIGURE 3.4: Top panel: Enclosed mass in DM and stellar content for the chosen IMFs for the galaxy cluster ABELL1068. Bottom panel: DM to stellar mass ratio. Note that the two contributions overlap around 1.5 kp, that is, the very inner region of the galaxy cluster.

This result suggests that it is very difficult to make a detailed study if the stellar content of the BCG because the gravitational lensing associated to it would be mostly caused by the dark matter component at almost all scales. The stellar content is only dominant in the innermost region, quite far from the Einstein radius which is constrained by the total enclosed mass (dark matter and stars).

It is then useful to study cases in which the lens system is an elliptical galaxy following its own dark matter halo and not inside the potential well of a galaxy cluster in the case of the BCG. If we now do the calculations for a galaxy with a characteristic radius of $r_s = 25.2$ kpc and concentration parameter $c = 7.94$ we get:

IMF/Method	Mass ($M_\odot$)
Salpeter	2.62×10^{11}
Kroupa	1.70×10^{11}
Chabrier	1.6×10^{11}
DM Halo	3.3×10^{12}

And the radial profiles in the case of the galaxy are shown in Figure [3.5], where the overlapping happens in a larger radius.

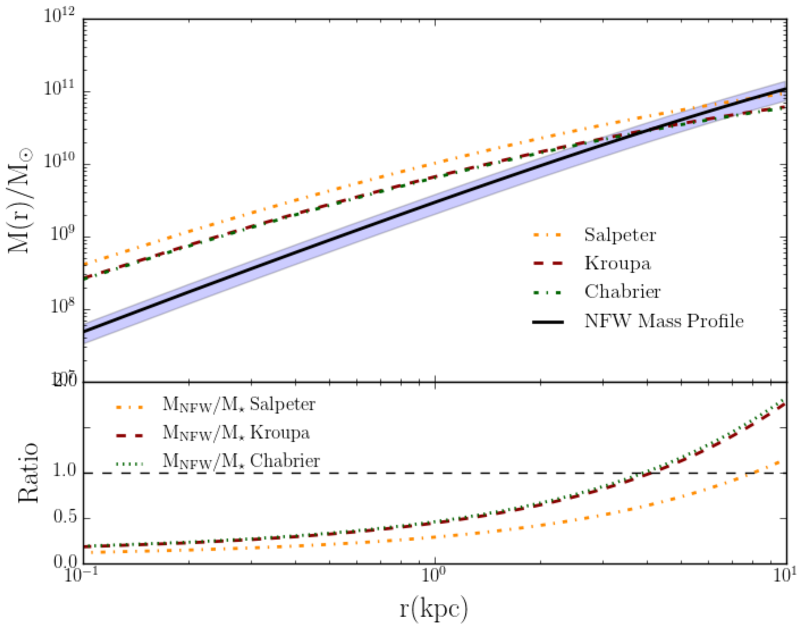

FIGURE 3.5: Top panel: Enclosed mass in DM and stellar content for the chosen IMFs for an early type galaxy. Bottom panel: DM to stellar mass ratio. The two contributions overlap around 3 kp, further from the center than in the case of the galaxy cluster.

Our result is in good concordance with the alalysis made by Sonnenfeld et. al. (2012) in the system SDSSJ0946+1006, also known as the "Jackpot". The overlapping of both contributions is around is 3 kp which is a larger radius than the one calculated for a BCG, (see Figure [3.6] for his results). The values for Sonenenfield's galaxy are $z = 0.222$, $c = 10^{0.9} = 7.9428$, $\delta_c = 25644.5$, $M_\star = 5.5 \times 10^{11} M_\odot$.

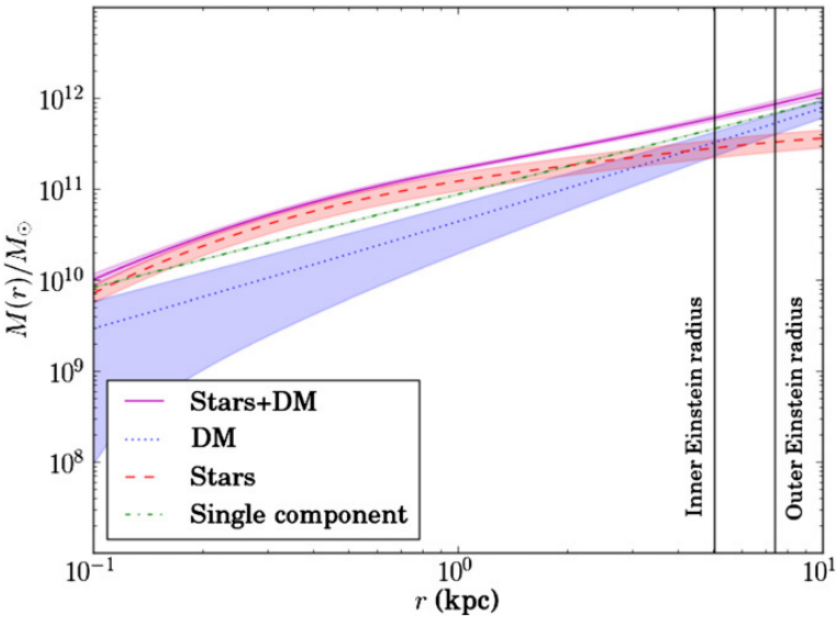

FIGURE 3.6: Mass profile for dark matter and stellar content for the lens system SDSSJ0946+1006. (Sonnenfeld et. al. 2012). The overlapping of DM and stellar content is in good agreement with our calculations.

This first results mean that the proper determination of the light of the BCG (and thus tracking their formation history through an accurate determination of their IMFs) is harder to do in the inner region of galaxy clusters than it is in early type galaxies in different spatial locations. Dark matter seems to be the overwhelming dominant contribution in the bright galaxies even in the inner regions.

3.3 Einstein Radius

Another way to constrain the relevant scales in which we might expect to see lensed objects is by analysing the Einstein radius because it is around this radial distance from the center of the BCGs that we expect to find arcs or multiple images of background objects, as displayed in Figure [3.7].

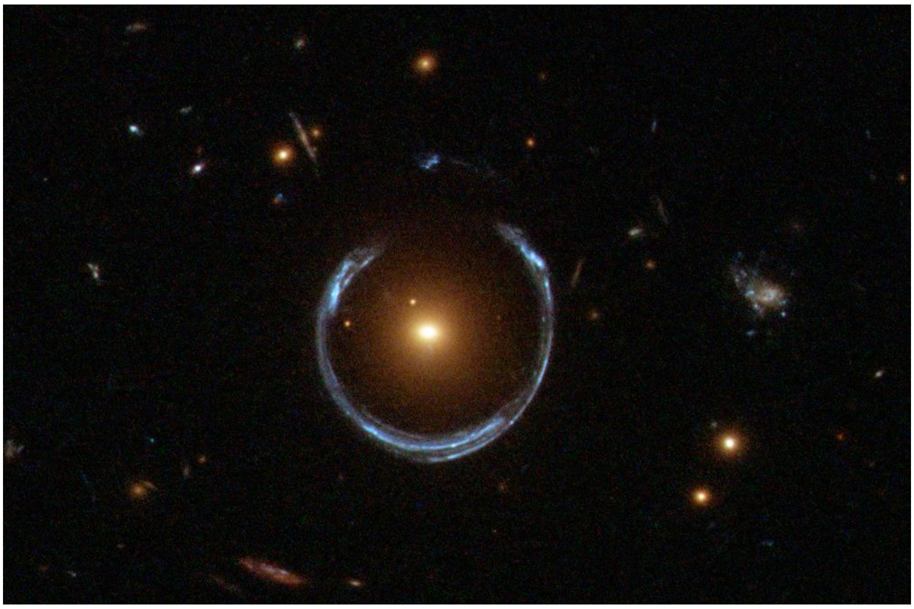

FIGURE 3.7: Einstein Ring in LRG 3-757 obtained by the Hubble Space Telescope. The distortion produced by the foreground galaxy (z=0.4457) is such that the light of the background galaxy (z=2.379) is stretched along the Einstein radius as well as being magnified. Image from Wikipedia.

Since we are interested in having an accurate estimate of the Einstein radius for different objects located at different redshifts, it is useful to calculate the shear, reduced shear and magnification (introduced in Chapter 2). Again, we make this calculations for the cluster Abell 1068.

The reduced shear is given by:

$$g = \frac{\gamma}{1-\kappa} \tag{3.4}$$

The reduced shear for background objects at different redshifts is shown in Figure [3.8]. The radius in which the reduced shear diverges is where the Einstein radius would be located for each of the background objects at the different given redshifts.

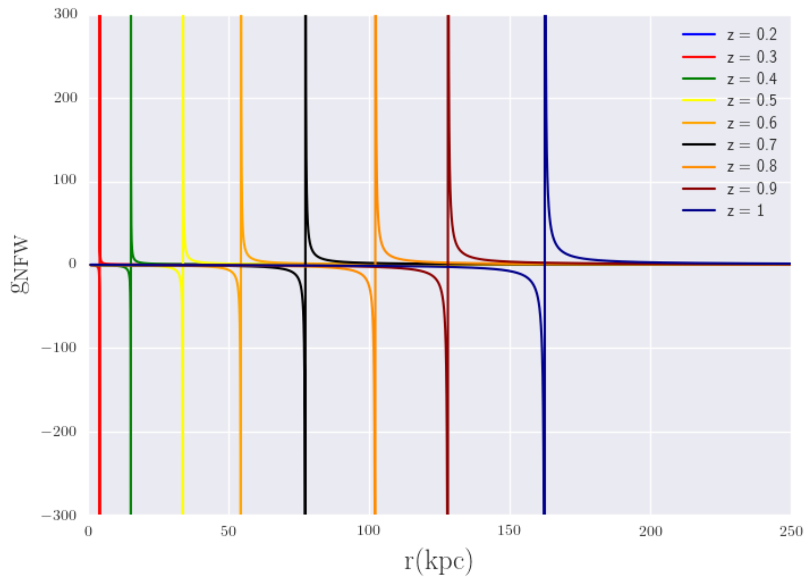

FIGURE 3.8: Reduced shear radial profile for different redshifts. The divergence occurs in the location of the Einstein ring.

Another useful way to constrain the Einstein radius is through the magnification given by equation (2.18)

Figure [3.9] shows the magnification. The infinite magnification happens in the Einstein radius so this is also a useful plot for the radial scales in which we might expect to find lensed galaxies.

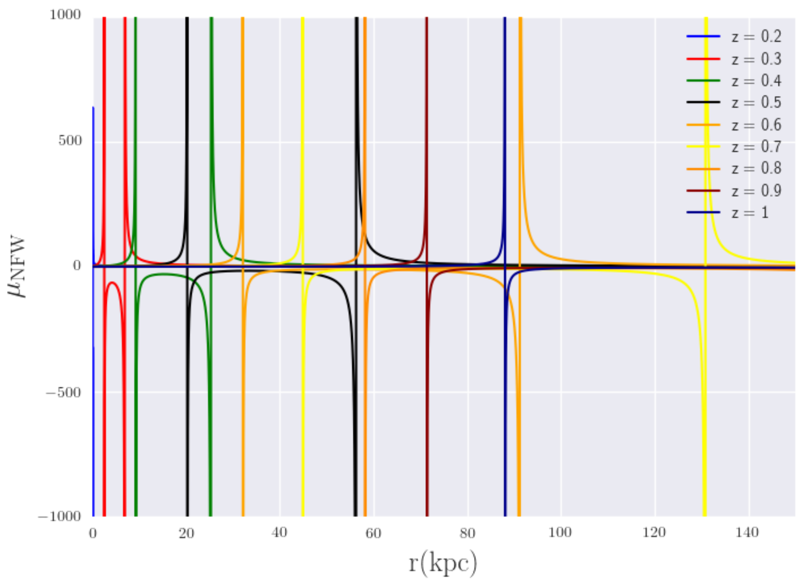

FIGURE 3.9: Magnification radial profile for various redshifts. Divergence occurs in the Einstein ring.

Taking into account the COSMOS catalogue experiment, and the plots for the reduced shear and the magnification, we would expect to find at least 1 or 2 lensed galaxies near a radial distance from the center of about 15 kp, although we know that the enclosed mass at this range is already mostly given by the DM halo.

Chapter 4

Data and analysis

For this project we make use of good quality deep data of galaxy clusters observed with the MegaCam wide field imager on the CFHT (Canada-France-Hawii Telescope). The cluster sample consisted of 101 clusters within the range of redshifts from $0.05 < z < 0.55$. The full description of this survey can be found in: Sand et. al. (2011)

58 clusters from the MENEACS (Multi-Epoch Nearby Cluster Survey). The MENEACS clusters represent all clusters in the BAX X-ray cluster database that are observable for the CFHT and this part of the data is in the g and r bands. We also make use of the INT data of the same cluster in the bands i and U.

After filtering out some of the clusters because of a very complex and crowded central region or just not good quality we used 30 clusters for the final studies and paid special attention to 10, marked with * in table 4.1.

The original images have dimensions of [11000:11000] pixels but since our relevant region is the center of the cluster where the BCG is located, we cut the images with dimension of [1000,1000] for the color analysis and [4000:4000] to characterize the colors and discriminate between cluster and non-cluster members.

Cluster	z	$\sigma(km/s)$	$d(Mpc)$	$\theta_E('')$
A1033	0.126	762	540	14.6155
A1068*	0.138	740	591.4	13.5945
A1132	0.136	727	582.9	13.1515
A119*	0.044	875	188.6	21.0798
A1413*	0.143	881	612.9	19.1569
A1650	0.084	720	360	13.6758
A1651	0.085	903	364.3	21.4876
A1795	0.062	778	265.7	16.3514
A2029*	0.077	1152	330	35.2776
A2050	0.118	854	505.7	18.5258
A2055	0.102	697	437.1	12.5642
A2064	0.108	675	462.9	11.7048
A2065*	0.073	1095	312.9	32.0110
A2069	0.116	966	497.1	23.7574
A2142*	0.091	1086	390	30.8756
A2319*	0.056	1101	240	32.9563
A2420	0.085	800	364.3	16.8653
A2440	0.091	766	390	15.3608
A2597	0.085	682	364.3	12.2569
A2627	0.126	800	540	16.1096
A2703	0.114	800	488.6	16.3307
A399	0.072	800	308.6	17.1049
A553	0.066	800	282.9	17.2155
A655*	0.127	800	544.3	16.0911
A754*	0.054	800	231.4	17.4367
A763	0.085	800	364.3	16.8653
A795	0.136	800	582.9	15.9252
A85*	0.055	800	235.7	17.4182
A961	0.124	800	531.4	16.1464
A990	0.144	800	617.1	15.7778

TABLE 4.1: Abell clusters used in this work. Marked with * the chosen clusters with the most promising features. From left to right: Name of the cluster, redshift, velocity dispersions from Sifon et. al. (2012), distance in Mpc and Einstein Ring using a single isothermal sphere as first approximation.

The INT images were obtained using multiple exposures so it was necessary to make a mosaic of them using `SWARP` Bertin et. al. (2002), so at the end we had the data of the clusters in the bands g,r,U,i with the same spatial scale. The first step in the removal of the light from the BCG was constructing a mask file (segmentation file) to only extract the desired galaxy, this was done using SEXTRACTOR (Bertin & Arnouts 1996).

The procedure is the following: SEXTRACTOR identifies the bright objects and extracts them while doing aperture photometry on them, the user can choose to obtain an examination image to see the extracted objects (that in our case would be the segmentation file). SEXTRACTOR labels each of the extracted regions with growing numbers where 1 is the brightest object (in most cases the BCG) so we can use python scripts to modify the segmentation file to mask only the galaxies but not the BCG which we want to fit properly. Figure [4.1] shows the original segmentation image and the one where the BCG light has been removed so that it won't be masked once we fit the light of the BCG (cluster Abell 754).

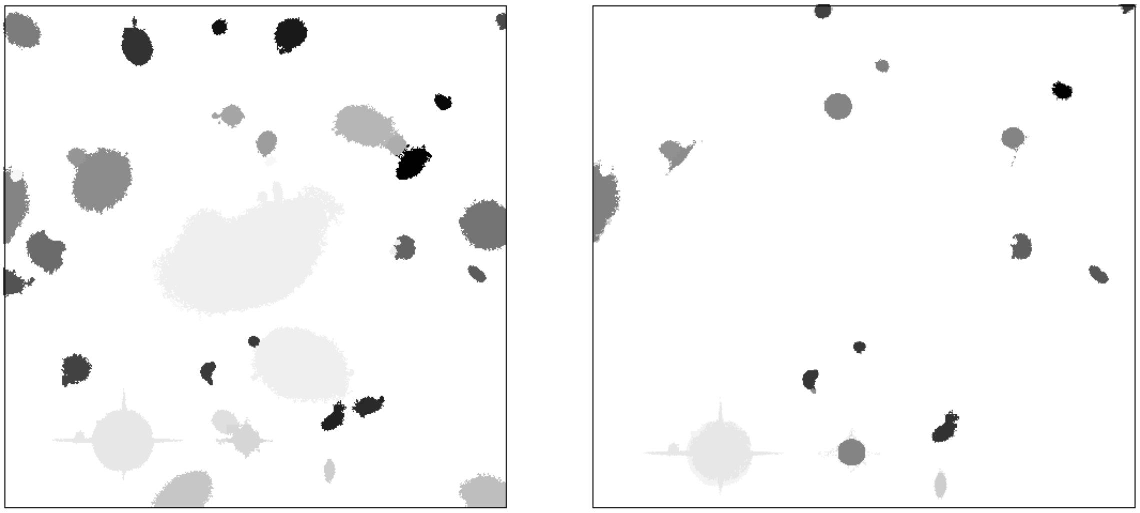

FIGURE 4.1: Segmentation images produced by SEXTRACTOR and used as mask files for the galfit extraction on the cluster Abell 754. Left panel is the original mask with all the bright objects. Right panel is the mask after the subtraction of the regions surrounding the cluster galaxies to be fitted with GALFIT. The colors are inverted for an easier visualization of the image. The fainter regions are actually the most luminous objects because GALFIT assigns increasing numbers starting from the brightest one, that is the BCG in this case.

Now, once the mask file is ready we can do the substraction of the BCG light using GALFIT (Peng et. al. 2002) which fits two dimensional profiles of galaxies (with different shapes and features). The first subtraction for most of our target clusters was done fitting a Sersic's profile with $n = 4$ which is de Vaucouleurs profile. Although in all cases some parameters such as the n index, the effective radius, Fourier and bending modes were to be changed and modified accordingly. A first run of GALFIT gives us a rough idea of the true position of the center of the BCG so we can set this values in a second run for each cluster.

We use the segmentation masks given by SEXTRACTOR to mask bright objects in the fitting of the BCG but in some cases it was necessary to do the fitting of many objects (not only the BCG). The best results were given when we also masked the innermost region of the BCG (the size of the seeing) so the fitting will put more weight in the rest of the profile, thus reducing most of the light that hides the background objects.

The power of `GALFIT` lies in the fact that it allows for different shape fitting through Fourier and bending modes. These parameters (`C0, B1, B2, F1, F2`, etc.) are hidden from the user unless he/she explicitly requests them. These can be tagged on to the end of any previous components except, of course, the PSF and the sky.

Some of the useful parameters that we used to properly fit the BCG in every case were: `B1)` Bending mode 1 (shear term), `B2)` Bending mode 2 (banana shape) `B3)` Bending mode 3 (S-shape) and for the azimuthal fourier modes $\texttt{F}_i$`)` Az. Fourier mode i where i can go up to a 20th Fourier mode, `C0)` traditional diskyness(-)/boxyness(+).

Figure [4.2] shows the original image, the fitted models and the output given by `GALFIT` for the cluster Abell 754. Note that many galaxies were fitted and many background objects can be seen near the center of the BCG.

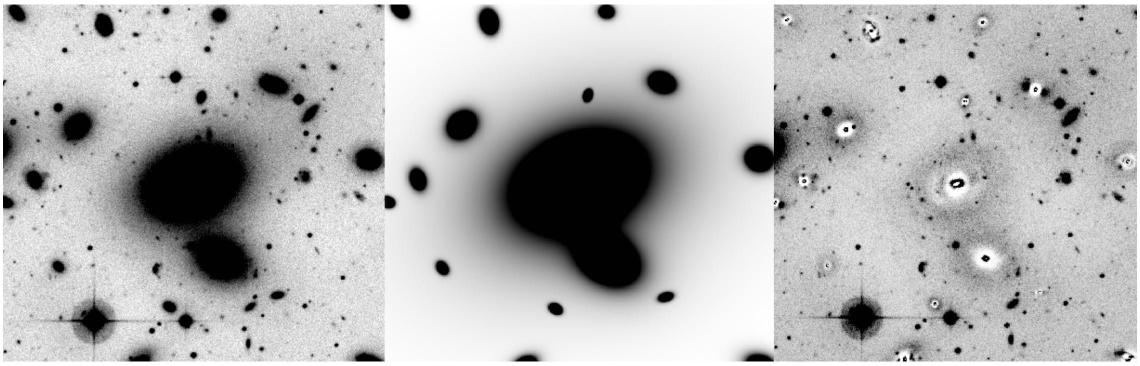

FIGURE 4.2: Galfit procedures. Left: Original image in "zscale" with the clear BCG expanding across a significant region of the central area. Middle: The models fitted by `GALFIT` for all the selected cluster galaxies. Right: Residual image after the subtraction of the model galaxies.

The same for cluster Abell 1413:

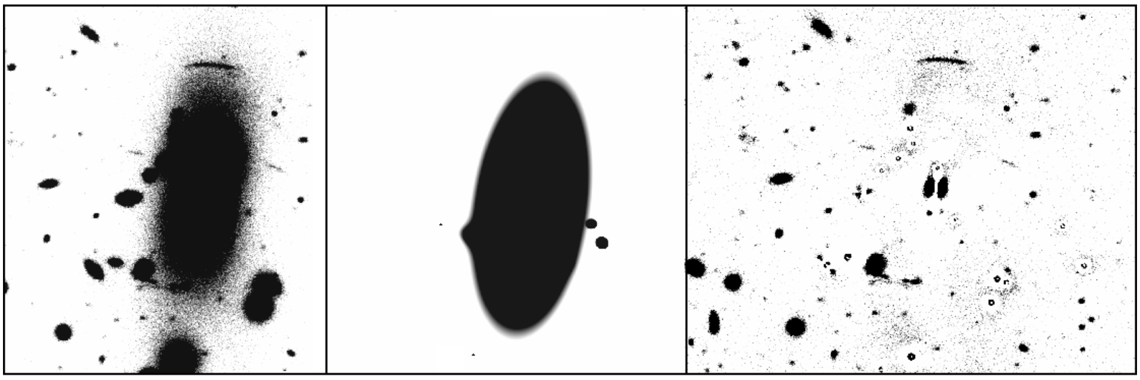

FIGURE 4.3: Galfit procedures on A1413. Left: Original image in "zscale" with the clear BCG expanding across a significant region of the central area. Middle: The models fitted by `GALFIT` for all the selected cluster galaxies. Right: Residual image after the subtraction of the model galaxies.

4.1 Color images

We use `IRAF` to make the color images using our g,r,U,i bands. Let's keep using Abell 754 which is a low redshift galaxy ($z = 0.054$) cluster with a calculated mass of $M_{200} = 9.8 \times 10^{15} M_\odot$ (Sifon et. al. 2015)

Here we take an isothermal sphere to model the Einstein ring for an assumed distance of background objects of $z = 0.5$. We made a color image of the original center of the cluster without subtracting the BCG in order to differentiate between cluster members from background galaxies and field stars. This allows us to fit only the cluster galaxies.

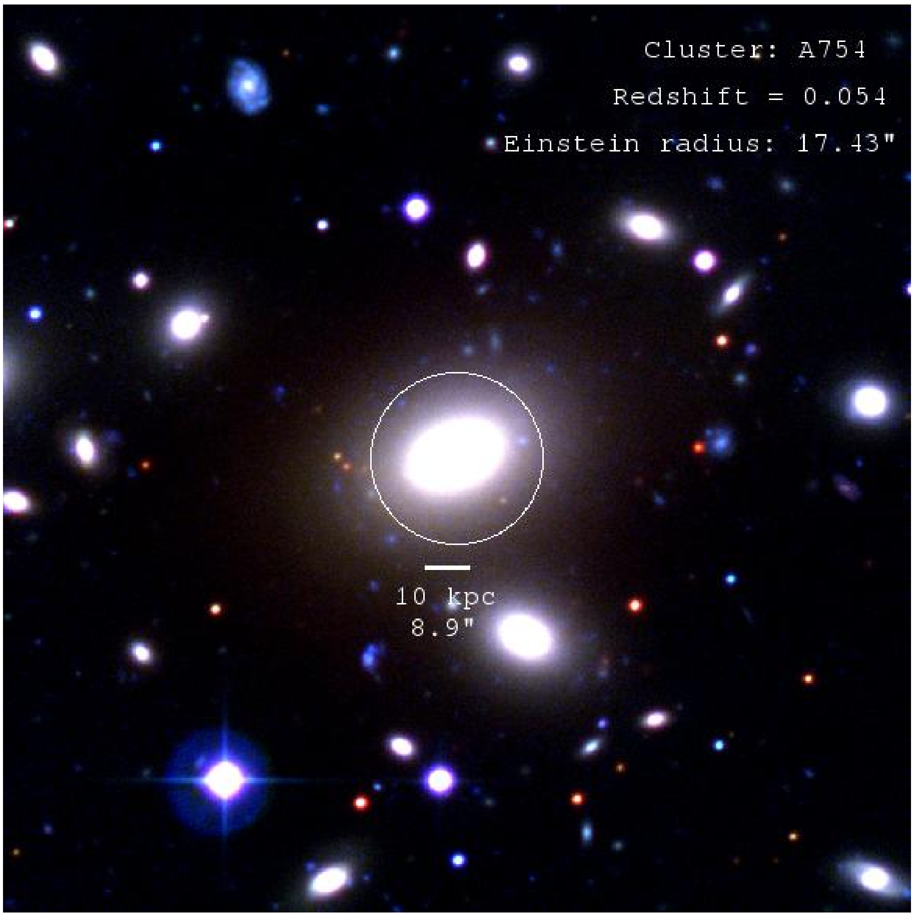

FIGURE 4.4: Color image of A754 cluster (filters i,g,U) with its Einstein radius calculated for an isothermal sphere of a background object at $z = 1$.

After choosing the galaxies that belong to the cluster by comparing their relative colors, we subtracted them using `GALFIT` and made the color image again changing the scaling values with the task `CONVERT` of `IRAF` so that we see can see the color contrast to search for good candidates of lensed objects. By looking at this reduced color image, we have another visual constraint to choose the clusters in which it would be worth to do photometric redshifts and search for objects with the same redshift in different locations around the very center of the BCG (object that has suffered strong lensing).

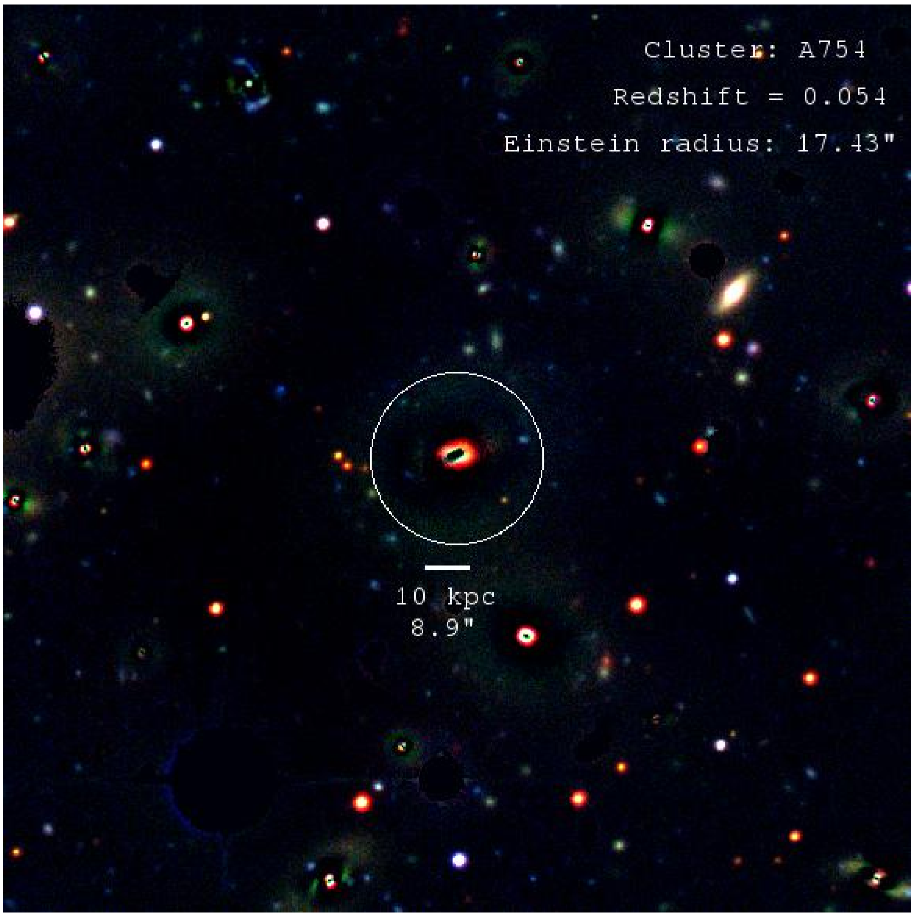

FIGURE 4.5: Color image of A754 cluster (filters i,g,U) after the subtraction of the bright cluster galaxies.

The irg color image of the cluster A1413: (this needs to be fixed)

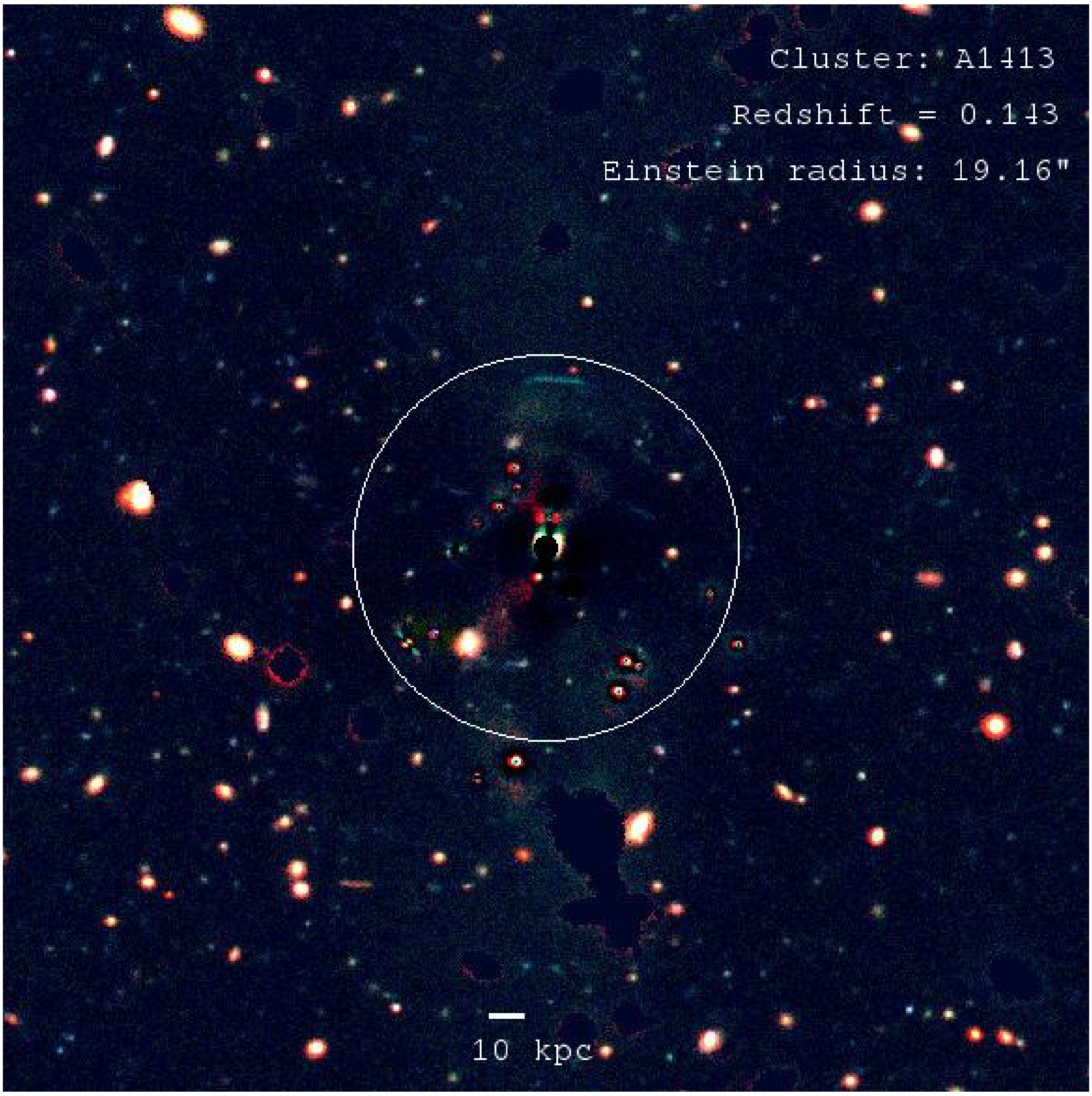

FIGURE 4.6: Einstein ring in color image of A1413.

Because we have 4 bands we were able to make different color images to see the contrast and make combinations that would allow us to see better the very red and very blue objects, hoping to find objects with the same colors that would be good candidates for lensed objects. Figure [4.5] displays the g-r, i-r-g and i-g-U color images for three clusters (Abell 961, Abell 2703 and Abell 1033).

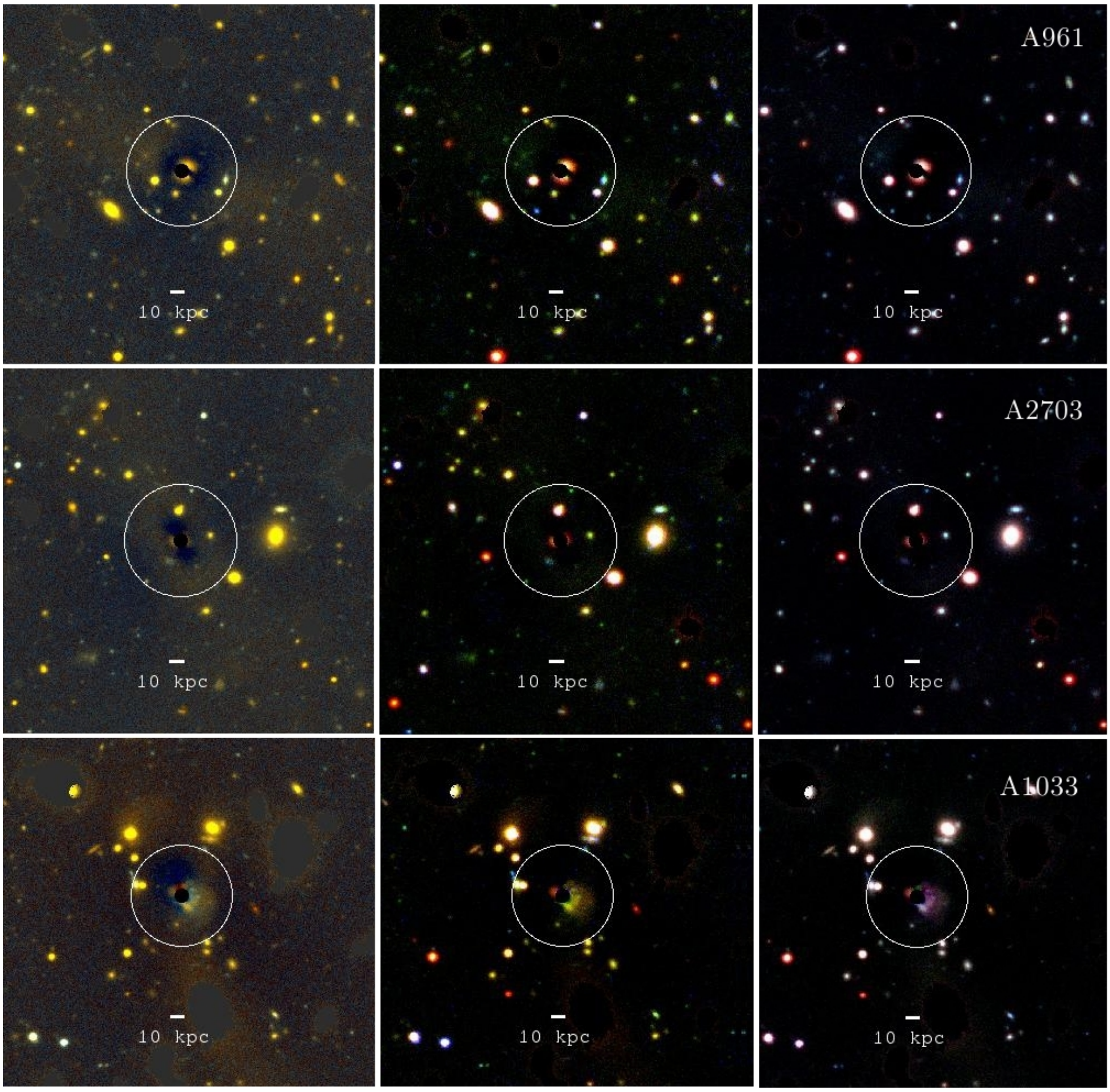

FIGURE 4.7: Different color images for different combination of the g,r,U,i filters for the clusters A961, A2703, A1033. Left column for the images constructed only with the g and r filter, central column for i,g,r and right column for i,g,U.

4.2 Photometric Redshifts

Using photometry data to get redshifts (Photometric redshifts) is not only a useful method to get redshifts of fainter objects than accesible by spectroscopy, but also the efficiency in terms of the number of objects with redshift estimates per unit telescope time is lagerly increased. Given the characteristics of our data, getting photo-z's of the background objects after the substraction of the BCG's could in principle help us find lensed objects (background galaxies with the same redshift located at different location could be lensed candidates).

The first step in determining the photometric redshifts is to discriminate between field stars and the galaxies of the clusters so in order to do this, we used some of the parameters found by `SEXTRACTOR` that allow us to constraint the fitted data. These are `class-star`, `flux_radius`, and `FWHM` (full wicth half maximum). Class-star uses the neural network star/galaxy of `SEXTRACTOR` that will give values close to 1 for stars and 0 for galaxies. `flux_radius`, and `FWHM` are closely related to each other and give the radius which contains half of the light of the object so it will be small for stars and bigger for extended objects.

In order to extract the same objects and make the segmentation masks for the desired objects in the different filters, we used `SEXTRACTOR` on dual mode and made aperture photometry on each of the relevant objects. Figure [4.6] shows the color magnitude diagram for Abell 754 where we used a zero point magnitude of 30.

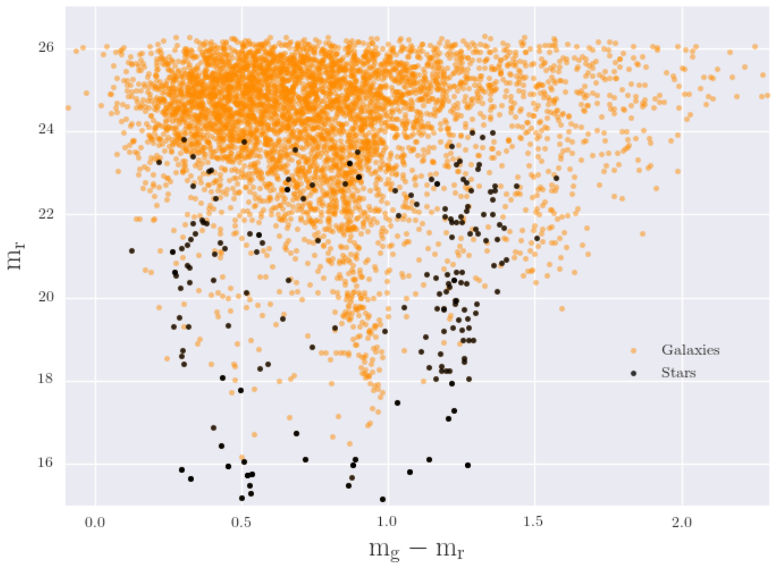

FIGURE 4.8: Color Magnitude diagram of Abell 754 with the differentiation of stars from galaxies.

We can also discriminate the stars from galaxies using the radius that contains most of the flux. Figure [4.7] shows the galaxies and stars in the Mag vs `Flux_rad` plane.

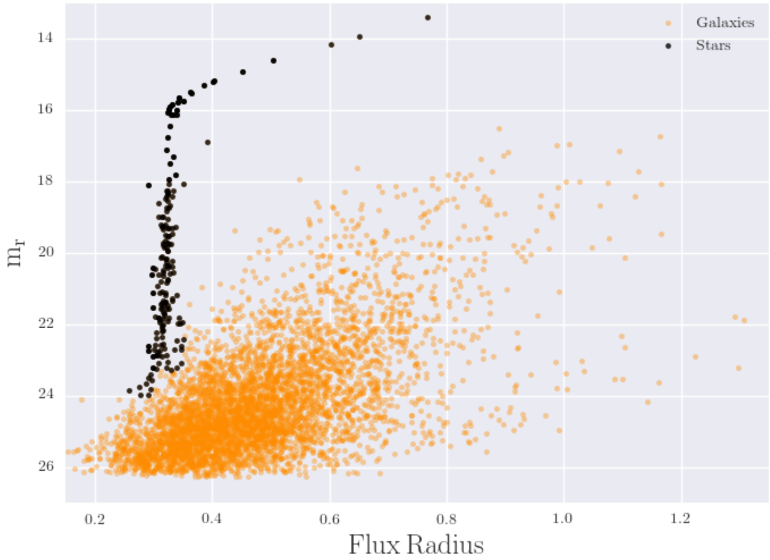

FIGURE 4.9: Magnitude vs Flux radius of Abell 754 to identify the galaxies using the criteria of their flux distribution.

Once we have selected only the magnitudes of the galaxies in our four filters, we can measure the photometric redshift of the galaxies in the inner region of the cluster after the subtraction of the BCG, we use the photometric redshift code `EAZY` by Brammer et. al. (2008) which uses an extensive collection of spectral energy distributions for galaxies in the range $0 < z < 4$. Fortunately, the code includes library from CFHT in the i and U bands but doesn't have the filters in the g and r bands so we used the SUBARU survey filter information to be able to compute the photometric redshifts using four bands.

Chapter 5

Conclusions

We don't expect too many sources in our sample data since the amount of sources that can reach the telescope with a sensitivity of m=23 is rather small and the difficulty of removing the BCG can make it even harder.

The proper determination of the light of the BCG (and thus tracking their formation history through an accurate determination of their IMFs) is harder to do in the inner region of galaxy clusters than it is in early type galaxies in different spatial locations.

Dark matter seems to be the overwhelming dominant contribution in the bright galaxies even in the inner regions. It seems to be more densely packed in galaxy clusters than it is in isolated early type galaxies with their own dark matter halo.

Appendix

Isothermal Sphere

Summary of isothermal sphere:

$$\rho(r) = \frac{\sigma^2}{2\pi G r^2} \tag{1}$$

$$\Sigma(\xi) = \frac{\sigma^2}{2G\xi} \tag{2}$$

The Einstein radius:

$$\xi_E = 4\pi \left(\frac{\sigma}{c}\right)^2 \frac{D_{ds}}{D_s} \tag{3}$$

NFW profile formalism

The NFW density profile is

$$\rho(r) = \frac{\delta_c \rho_c}{(r/r_s)(1 + r/r_s)^2} \tag{4}$$

where the characteristic over density (dimensionless quantity) is given by:

$$\delta_c = \frac{200}{3} \frac{c^3}{\ln(1+c) - c/(1+c)} \tag{5}$$

The mass of an NFW halo contained within a radius of r_{200} is:

$$\mathrm{M}_{200} = \mathrm{M}(r_{200}) = \frac{800\pi}{3} \rho_c r_{200}^3 = \frac{800\pi}{3} \frac{\bar{\rho}(z)}{\Omega(z)} r_{200}^3 \tag{6}$$

The concentration parameter c is strongly correlated with Hubble type, c=2.6 separating early from late-type galaxies. Those galaxies with concentration indices $c > 2.6$ are early-type galaxies reflecting the fact that the light is more concentrated towards their centres, its formal definition in terms of the virial and characteristic radius is $c = r_{200}/r_s$.

Dutton & Maccio (2014) (in continuation of previous studies such as Muñoz Cuartas et. al. 2010), made simulations of halo masses from dwarf galaxies to galaxy clusters and find constraints on the concentration parameter for different redshifts, the relation between the concentration parameter with redshift and virial mass is shown in Figure [1].

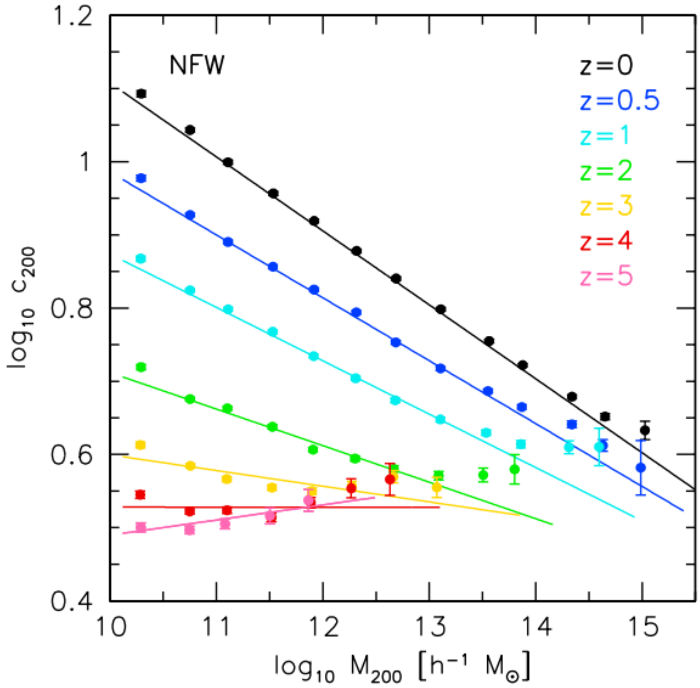

FIGURE 1: Evolution of the concentration mass relation, by Dutton & Maccio (2014).

The surface mass density in the NFW profile is given by:

$$\Sigma_{\rm NFW}(x) = \begin{cases} \frac{2r_s\delta_c\rho_c}{(x^2-1)}\left[1 - \frac{2}{\sqrt{1-x^2}}\,\text{arctanh}\sqrt{\frac{1-x}{1+x}}\right] & (x < 1) \\ \frac{2r_s\delta_c\rho_c}{3} & (x = 1) \\ \frac{2r_s\delta_c\rho_c}{(x^2-1)}\left[1 - \frac{2}{\sqrt{x^2-1}}\,\arctan\sqrt{\frac{x-1}{1+x}}\right] & (x > 1) \end{cases} \tag{7}$$

so from the critical density:

$$\rho_c = \frac{3H^2(z)}{8\pi G} \tag{8}$$

$H(z) = H_0(1 + \Omega z)^{3/2}$

But we are more interested in the enclosed mass which can be done by integrating the surface mass density:

$$\mathrm{M}(R) = \int_0^R 2\pi R \Sigma(R) dR \tag{9}$$

The radial dependence on the shear is:

$$\gamma_{\mathrm{NFW}}(x) = \begin{cases} \frac{r_s \delta_c \rho_c}{\Sigma_c} g_<(x) & (x < 1) \\ \frac{r_s \delta_c \rho_c}{\Sigma_c} \left[\frac{10}{3} + 4 \ln\left(\frac{1}{2}\right)\right] & (x = 1) \\ \frac{r_s \delta_c \rho_c}{\Sigma_c} g_>(x) & (x > 1) \end{cases} \tag{10}$$

where:

$$g_<(x) = \frac{8 \,\mathrm{arctanh} \sqrt{\frac{1-x}{1+x}}}{x^2 \sqrt{1-x^2}} + \frac{4}{x^2} \ln\left(\frac{x}{2}\right) - \frac{2}{(x^2-1)} + \frac{4 \,\mathrm{arctanh} \sqrt{\frac{1-x}{1+x}}}{(x^2-1)(1-x^2)^{1/2}} \tag{11}$$

$$g_<(x) = \frac{8 \arctan \sqrt{\frac{x-1}{1+x}}}{x^2 \sqrt{x^2-1}} + \frac{4}{x^2} \ln\left(\frac{x}{2}\right) - \frac{2}{(x^2-1)} + \frac{4 \arctan \sqrt{\frac{x-1}{1+x}}}{(x^2-1)^{3/2}} \tag{12}$$

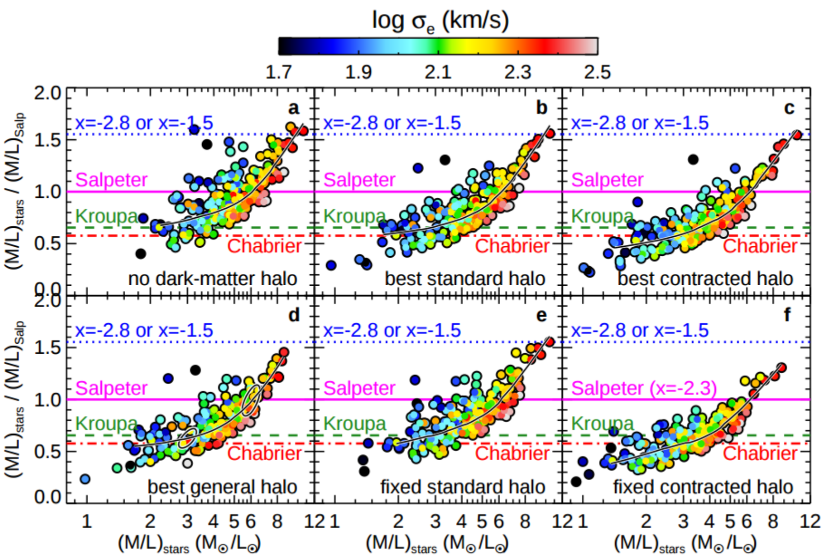

FIGURE 2: The systematic variation of the IMF in early-type galaxies, Cappellari et. al. (2012).

Bibliography

[1] John. Smith, Russell & Lucey. A giant elliptical galaxy with a lightweight initial mass function. *MNRAS*, 000:1–14, 2013.

[2] Gilles Chabrier. Galactic stellar and substellar initial mass function. *The Astronomical Society of the Pacific*, 115:763–795, 2003.

[3] Pavel Kroupa. On the variation of the initial mass function. *MNRAS*, 322:231–246, 2001.

[4] Brewer et. al. The swells survey. vi. hierarchical inference of the initial mass functions of bulges and discs. *MNRAS*, 000:1–13, 2012.

[5] R. F. J. Van der Burg et. al. Evidence for the inside-out growth of the stellar mass distribution in galaxy clusters since $z \approx 1$. *preprint arXiv:1412.2137v2*, 2015.

[6] Navarro. Frenk & White. The structure of cold dark matter halos. *The Astrophysical Journal*, 462:563–575, 1996.

[7] Thomas. J et. al. Massive elliptical galaxies: Bh scouring or bottom-heavy imf. *Proceedings IAU Symposium*, (311), 2014.

[8] Tommaso Treu. Strong lensing by galaxies. *Annual Review of Astronomy ans Astrophysics*, 48:87–125, 2010.

[9] Matthew R. George et. al. Galaxies in x-ray groups. ii. a weak lensing study of halo centering. *The Astrophysical Journal*, 757:2–18, 2012.

[10] D. Harvey et. al. A detection of wobbling brightest cluster galaxies within massive galaxy clusters. *MNRAS*, 000:1–9, 2017.

[11] Ramesh. et. al. Narayan. Lectures on gravitational lensing. *Proceedings of the 1995 Jerusalem Winter School. Cambridge University Press*, 1995.

[12] F. et. al. Courbin. Quasar lensing. *Lecture Notes in Physics, Berlin Springer Verlag*, 608:1, 2002.

[13] Massimo Meneghetti. Introduction to gravitational lensing. *Lecture Scripts, Heildelberg University*, 2003. URL http://www.ita.uni-heidelberg.de/~massimo/sub/Lectures/gl_all.pdf.

[14] Teresa. C. O. Wright & Teresa G. Brainerd. Gravitational lensing by nfw halos. *preprint arXiv:astro-ph/9908213v1*, 1999.

[15] Laigle et. al. The cosmos2015 catalog: Exploring the 1¡z¡6 universe with half a million galaxies. *The Astrophysical Journal*, 224(2), 2016.

[16] Gerard de Vaucouleurs. Sur la technique de l'analyse microphotometrique des nebuleuses brillantes. *Recherches sur les nebuleuses extragalactiques*, 1948.

[17] Ewa L. Lokas & Gary A. Mamon. Properties of spherical galaxies and clusters with an nfw density profile. *MNRAS*, 321:155–166, 2001.

[18] C. Sifon et. al. Constraints on the alignment of galaxies in galaxy clusters from ˜14000 spectroscopic members. *A& A*, 575:A48, 2015.

[19] A. Sonnenfeld et. al. Evidence of dark matter contraction and a salpeter initial mass function in a massive early-type galaxy. *The Astrophysical Journal*, 752:163–180, 2012.

[20] D. J. Sand et. al. Intracluster supernovae in the multi-epoch nearby cluster survey. *The Astrophysical Journal*, 729:142–155, 2011.

[21] C. Bildfell et. al. Evolution of the red sequence giant to dwarf ratio in galaxy clusters out to $z \approx 0.5$. *MNRAS*, 425:204–221, 2012.

[22] Bertin et. al. The terapix pipeline. *Astronomical Data Analysis Software and Systems XI*, 281, 2002. URL http://adsabs.harvard.edu/abs/2002ASPC..281..228B.

[23] Bertin. E & Arnouts. S. Sextractor: Software for source extraction. *Astronomy and Astrophysics*, 117:393–404, 1996.

[24] Peng et. al. Detailed structural decomposition of galaxy images. *The Astronomical Journal*, 124:266–293, 2002.

[25] van Dokkum Brammer and Coppi. Eazy: A fast, public photometric redshift code. *ApJ*, 686(1503), 2008.

[26] Dutton & Maccio. Cold dark matter haloes in the planck era: evolution of structural parameters for einasto and nfw profiles. *MNRAS*, 441:3359–3374, 2014.

[27] J. C. Mu noz Cuartas et. al. The redshift evolution of λcdm halo parameters: concentration, spin and shape. *MNRAS*, 000:1–11, 2010.

[28] Cappellari et. al. Systematic variation of the stellar initial mass function in early-type galaxies. *Nature*, 484:485–488, 2012.